Research Article

Experimental and computational investigation of PVDF–$BaTiO_3$ interface for impact sensing and energy harvesting applications

Dinesh Ramesh[1] · Nandika D'Souza[1,2]

Received: 20 September 2019 / Accepted: 16 April 2020

Abstract
The interfacial polarization between PVDF and $BaTiO_3$ was studied using density functional theory calculations and atomic charge density analysis. A comparative study of dielectric relaxation, thermodynamic properties and impact analysis of the electrospun polyvinylidene fluoride (PVDF) and a 3% $BaTiO_3$–PVDF nanofibrous composite are presented. The frequency-dependent dielectric properties revealed the microstructural feature of the composite material. The impedance analysis and Nyquist plots showed a decrease in the bulk resistance of the composite compared to the pure PVDF. The temperature dependence of the electric modulus shows Arrhenius-type behavior. The electric loss modulus relaxation peak shifts towards the high frequency side which indicates a decrease in relaxation time and faster charge carrier dynamics. The observed non-Debye type dielectric relaxation in electric loss modulus follows a thermally activated process, which can be attributed to the polaron hopping effect. The particle-induced crystallization of the PVDF polymer is supported by thermodynamic properties from differential scanning calorimetric measurements. The observed increase in piezoelectric response from high strain rate impact sensing was attributed to the interfacial interaction between PVDF and $BaTiO_3$.

Keywords Polymer–ceramic interface · Polaron hopping · Flexible piezoelectrics · Impact sensing

1 Introduction

Flexible bioinspired materials are an emerging area of research, especially for wearable, IoE (Internet of Everything), real-time health monitoring [1–4] and energy harvesting applications [5]. PVDF–$BaTiO_3$ composite material is an excellent choice for making flexible sensors with real-time health monitoring applications [6]. PVDF is a semicrystalline polymer [7], and due to its piezoelectric behavior, it has potential applications for making flexible piezoelectric sensors and generators [8, 9]. $BaTiO_3$ is an important member of the lead-free perovskite compounds [10]. At room temperature, $BaTiO_3$ has the tetragonal crystal structure having spontaneous polarization. The origin of spontaneous polarization in the absence of applied field can be explained on the basis of distortion in the crystal structure resulting in the absence of the center of symmetry. By adding $BaTiO_3$ as a ceramic filler, the composite's dielectric permittivity can be increased [11, 12]. The unusual piezoelectric property of the resulting composites [13] can also find use in high-energy-density capacitors [14] and flexible bionic energy harvesters [15, 16].

PVDF–$BaTiO_3$ nanocomposite system has been studied with different processing techniques including melt processing [17], solution casting [18, 19], molten salt method [20], compression molding [21], sol–gel method [22],

Electronic supplementary material The online version of this article (https://doi.org/10.1007/s42452-020-2788-y) contains supplementary material, which is available to authorized users.

✉ Dinesh Ramesh, mail2dineshram@gmail.com | [1]Mechanical and Energy Engineering, University of North Texas, Denton, TX, USA. [2]Materials Science and Engineering, University of North Texas, Denton, TX, USA.

Published online: 27 May 2020

electrospinning [12, 17], reversible addition-fragmentation chain transfer (RAFT) [23] and additive manufacturing/3D printing [24, 25]. The 3D printing of hybrid materials with PVDF and $BaTiO_3$ showed nearly 20-fold increase in dielectric constant compared to the pure PVDF [25]. Other piezoelectric polymer composites have been made either by spin casting or drop-casting methods [26–28] for use in structural health monitoring applications. Two issues affect their viability. One is the need for post-manufacturing poling and another the difficulty with long term durability when they are attached using adhesives. We address the need for poling by using an electrospinning approach to fabricating the composites. The application of a high voltage, when the chains have high mobility in solution enables piezoresponse without poling [29]. We address the need for an adhesive through evaluation of flexible textile design. The resulting flexible sensing composite with a improved surface area/surface energy is capable of attachment to complex curved surfaces, without loss of sensitivity.

Electrospinning is a novel method for fabricating thin nanofibrous mesh with high surface area [30–32] and surface energy [29] eliminating the adherence issue, making it an excellent choice for preparing flexible impact sensors. Composites made by electrospinning process undergo mechanical stretching with high electric fields which provides a local poling, thereby increasing the crystallinity of the polymer. The increased crystallinity also increases the piezoelectric properties of the resulting composite. The electrospun mats can also be modified into smart fabrics with twisted yarn method [33]. Considering these advantages, electrospinning was used to prepare the PVDF–$BaTiO_3$ nanocomposite.

Fundamental understanding of the interfaces in the heterogeneous systems is very important in order to fine tune its properties. In the case of nanocomposites, the interfacial interaction between the ceramic filler and polymer plays a crucial role in determining the property of the material. Although the performance of the composite materials is often attributed to the interfacial interaction [34], there is no detailed atomic level description of the interface. This is due to the fact that the interfacial interaction at the atomic level is not directly observable using current state of the art characterization tools and DFT calculations. The density functional theory-based calculations followed by atomic charge density analysis can be used to provide useful information about the interface between the polymer and ceramic materials. To the best of our knowledge, there is no study on the interfacial interaction between the PVDF polymer and $BaTiO_3$. Here, for the first time, using a combined experimental and DFT approach, the interface between orthorhombic β-phase PVDF and tetragonal-$BaTiO_3$ has been explored.

The present work describes the Bader's charge analysis of the interface, to understand the atomic charge distribution at the interface region, dielectric relaxation, thermodynamic properties and impact sensing property of PVDF–$BaTiO_3$ nanofibrous composite. The increase in the piezoelectric property and dielectric response of the composite was correlated with the interfacial polarization, particle ($BaTiO_3$)-induced crystallization of the PVDF polymer and polaron hopping mechanism.

2 Experimental

2.1 Materials

The powder form of polyvinylidene fluoride (PVDF) polymer was purchased from Sigma-Aldrich (CAS Number 24937-79-9) with a average molecular weight of ~ 534,000 (Mw), density of 1.74 g/mL at 25 °C and the refractive index is 1.43 (n20/D). $BaTiO_3$ (FW 233.24) was obtained in powder form from Sigma-Aldrich (CAS Number 12047-27-7). The average particle size is < 3 micron with the purity of 99 % with a density of 6.08 g/cc at 25 °C. N, N-Dimethylformamide (DMF) (MW 73.09 g/mol) CHROMASOLV® Plus, for HPLC, ≥ 99.9% was purchased from Sigma-Aldrich (CAS Number 68-12-2) and was used as a solvent for dispersing $BaTiO_3$ and electrospinning.

2.2 Fabrication of nanofibrous electrospun mesh

The PVDF nanofibers and a 3% $BaTiO_3$ in PVDF nanofibrous polymer composite mesh were prepared via electrospinning process by using 20 kV applied voltage. The average particle size of $BaTiO_3$ is < 3 micron with the purity of 99 %. The 20 kV was selected based on trial and error approach to get nanometer sized fibers. The electrospinning solution was optimized using 2^k factorial design approach as reported in [29]. The concentration of ceramic filler was chosen as 3% to get uniform fibrous morphology. The concentration was chosen based on the feasibility of electrospinning process.

2.3 Density functional theory (DFT) calculations and Bader charge analysis

Although the monoclinic α-phase is the dominant phase among the four major polymorphs of PVDF ($\alpha, \beta, \gamma, \delta$) [35], the β-phase is desired due to its electroactivity. Electrospun PVDF–$BaTiO_3$ composite has a higher content of β -phase compared to the other processing routes like compression molding [29]. So, the orthorhombic β-PVDF was chosen for the interfacial studies. The tetragonal $BaTiO_3$ (P4mm) $\alpha = \beta = \gamma = 90$ °; a and b = 3.9999 Å , c = 4.0170

Å) and orthorhombic β-PVDF (Cm2m) $\alpha = \beta = \gamma = 90$ °; a = 8.6915 Å, b = 4.8929 Å, c = 2.5675 Å) were combined with lattice matched sites in an orthorhombic unit cell and relaxed. The two unit cells were combined using the lattice matching algorithm [36] as implemented in Atomistic toolkit software. This is to minimize the interfacial strain between the β-PVDF and $BaTiO_3$. The interfacial distance between β-PVDF and $BaTiO_3$ was 1.9482 Å.

The self-consistent DFT calculations were carried out using the real-space projector-augmented wave (PAW) method [37, 38] as implemented in GPAW [39, 40]. A real-space grid spacing of 0.18 Å was used. The Brillouin zone was sampled using the Monkhorst-Pack scheme [41]. All calculations were converged to a energy of < 0.5 meV. The Perdew–Burke–Ernzerhof (PBE) generalized gradient approximation functional [42] was used for these calculations. The chosen k-point grid were (4 × 4 × 4), (4 × 4 × 4) and (6 × 6 × 6) for $BaTiO_3$, PVDF and PVDF–$BaTiO_3$ systems, respectively.

The charge density on individual atoms in the systems were calculated using the algorithm implemented by Henkelman et al., [43, 44] based on the Bader partitioning scheme [45]. The charge density was calculated for isolated $BaTiO_3$, β-PVDF and compared with PVDF–$BaTiO_3$ system.

2.4 Scanning electron microscopy (SEM)

A FEI-Quanta Environmental SEM was used to get the lateral image of fibers. The analysis was carried out at low vacuum using a 15 kV beam current and 5.0 nm spot size. To prevent surface "charging" and to protect the sample surface from e-beam induced damage, a thin conducting layer with (60/40) Pd/Au alloy was sputter deposited on the sample surface as described in dielectric analysis in the following section.

2.5 Temperature and frequency-dependent dielectric analysis

Microstructure of the composite material was analyzed by dielectric analysis. Temperature and frequency-dependent dielectric spectroscopic measurements were carried out using TA instrument ARES strain-controlled shear rheometer and an E4980A LCR meter (Agilent technologies). The sample surface was coated with a blocking electrode of (60/40) Pd/Au alloy [46] using sputtering with Ar ion plasma. The purpose of the blocking electrode is to prevent the charge accumulation at the electrode/dielectric material interface. A Model 5100 from POLARON instruments Inc. was used to sputter the sample. The voltage and current were set at 2.5 kV and 5 mA. The plasma was initiated at 20 mA current and sustained for 2 min to coat a thin conducting layer to prevent the electron accumulation and to have a better electrical contact.

The electrospun mesh was cut into 24-mm (diameter) samples with the thickness of ≈ 0.55 mm, and the 24-mm parallel plate geometry of the rheometer was employed for dielectric analysis. During the frequency scan measurement, the Agilent multimeter applied 1V DC voltage to sample, to prevent the charge building up at the interface of the dielectric material and parallel plate electrodes. The applied DC voltage causes the molecules to align from a random orientation. By applying the AC sinusoidal voltage, the dielectric storage and loss can be measured. The frequency of the AC electric field was scanned from 20 Hz to 2 MHz. The samples were studied in the temperature range of 100–180 °C, because the melting point of PVDF is around 170 °C to 180 °C. The real and imaginary part of dielectric permittivity as a function of temperature at different frequencies was studied. The impedance and electric modulus were calculated from the dielectric permittivity values.

2.6 Differential scanning calorimetry (DSC)

The crystallization and melting behavior of electrospun PVDF fiber and PVDF–$BaTiO_3$ composite were investigated by using the Perkin Elmer DSC 6 in a nitrogen atmosphere. Approximately 4 to 6 mg of the sample was sealed in an aluminum pan. Heating and cooling scans were performed at 10 °C/min between 30 and 220 °C. Samples were held at 220 °C in the molten state for 5 min to eliminate previous thermal history prior to the cooling scan.

2.7 Piezoelectric analysis by impact measurement

The piezoelectric properties of the electrospun meshes were analyzed using impact analyses. The electrospun meshes were cut into 6.5 cm^2 and sandwiched between two copper plates of 1 mm thickness. The impacted force causes voltage generation in the material which was analyzed using the oscilloscope (Tektronix TDS 3054C). The experimental setup is given in supplemental Fig. S5.

The impact force on the electrospun mesh samples was imparted using a hand-held impulse force hammer (model 086C03 from PCB Piezoelectronics). The applied force was measured using the piezoelectric force transducer (Quartz) at the tip of the hammer. The measured output voltage (mV) due to impact force on the transducer was converted to force (N) using the following relation with the impact hammer's sensitivity value of 2.25 mV provided by the manufacturer.

$$\text{Force } (N) = \frac{\text{Voltage (mV)}}{2.25 \text{ mV/N}} \quad (1)$$

3 Results and discussion

Schematic representation of fabrication and multiphysics approach is shown in supplemental Fig. S1.

3.1 Interfacial charge distribution analysis

Firstly, the plane wave basis set was used for solving the time-independent Schrödinger equation (2) among the atoms in a stationary system.

$$\hat{H}\Psi = E\Psi \quad (2)$$

where $\hat{H}$ is the Hamiltonian operator and can be written as

$$[\hat{T}_e + \hat{V}_{en} + \hat{V}_{ee}]\Psi = E\Psi \quad (3)$$

where $\hat{T}_e$ is kinetic energy operator for electrons, $\hat{V}_{en}$ is the electron-nucleus interaction and $\hat{V}_{ee}$ is the electron-electron interaction, Ψ is the wave function and constant E defines the energy level of the system.

The output from this quantum mechanical calculation contains the plane wave function/electron charge density which is continuous. To get information such as polarization/charge distribution in atoms, it is essential to partition the electron charge density. Bader's partitioning scheme [45] applies a large grid to the charge density of atoms, and the partitioning algorithm [43, 44] follows the steepest ascent paths along the charge density gradient. When a charge density maximum is reached, the algorithm rejects the subsequent paths enabling the mapping of charge density distribution of the system under study. The charge distribution obtained from this analysis was plotted as 2D contour surface plots with heat map in Figs. 1b, 2b and 3b, respectively. The highest and the lowest points reflect the charge density being maximum and minimum.

The charge density contour plots suggest that, when PVDF and $BaTiO_3$ comes in contact, there is a transfer of charge at the interface. This results in Ba atoms which are close to the interface experiencing less screening from the electrons in the neighbor atoms, in the consequent higher charge density on Ba leads to a higher polarization.

This phenomenon is also consistent with the results from first principles calculations of atomic scale permittivity of the $C_{12}H_{25}$ molecule/SiO_2 interface [47], isotactic-polypropylene/Al_2O_3 and isotactic-polypropylene/$PbTiO_3$ interfaces [48] where an increase in optical and static permittivity values at the interfaces were reported.

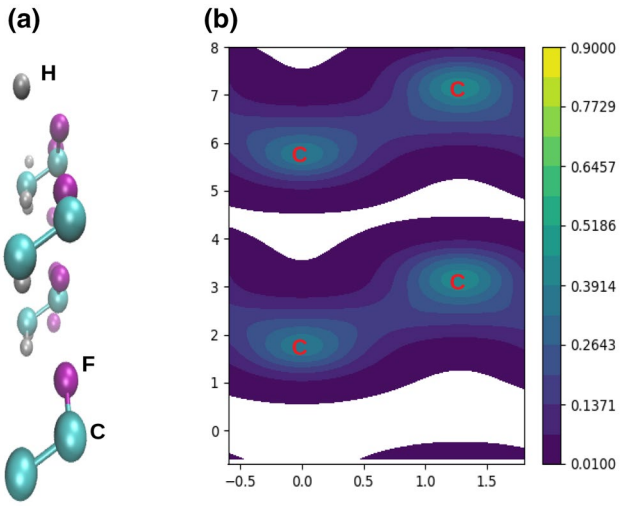

Fig. 2 **a** Orthorhombic β-phase PVDF, **b** Bader charge analysis of β-phase PVDF

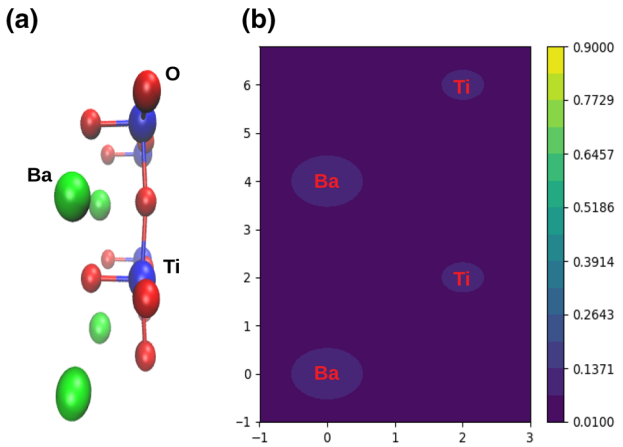

Fig. 1 **a** Tetragonal $BaTiO_3$, **b** Bader charge analysis of $BaTiO_3$

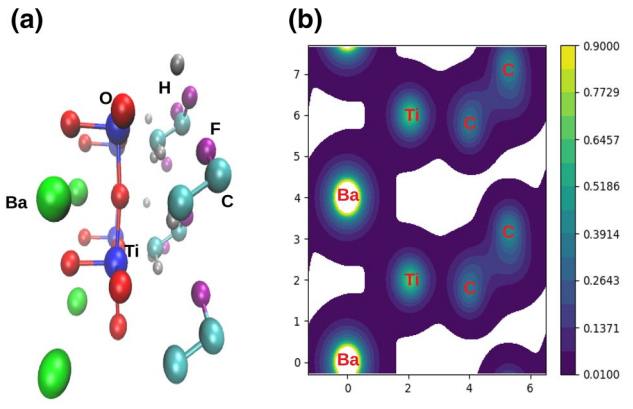

Fig. 3 **a** Tetragonal $BaTiO_3$-β-PVDF system, **b** Bader charge analysis of interface between $BaTiO_3$ and β-phase PVDF

3.2 Morphology and microstructural analysis of PVDF-$BaTiO_3$ electrospun composite

The gecko toe pads consist of a complex microstructure with long hairs called setae which further branches out into a fibrillar structure called spatulae. The diameter of these fibers are on the order of 200 nm to 400 nm making their sticky toe to climb on any surfaces [49]. The diameter of the electrospun PVDF–$BaTiO_3$ fibers were optimized to produce fibers in the range of 200 nm to 400 nm. This unique mesoscale morphology will aid in solving the adherence issue of spin/drop cast films with complex/curved surfaces. The SEM pictures were analyzed using Image J [50] and given in supplemental Fig. S2. The average fiber diameter of PVDF mesh was ≈ 850 nm and the PVDF–$BaTiO_3$ composite was ≈ 250 nm as reported in our previous studies [29].

3.3 Molecular structural analysis and charge dynamics by dielectric characterization

To understand the relaxation effect and interfacial interaction between the PVDF and $BaTiO_3$ in the electrospun composite material, it is important to understand the basic polarization mechanisms, present in a dielectric material. When a dielectric material is subjected to an applied electric field, the positive and negative charges in the material become polarized to compensate for the applied electric field, causing a net polarization in the material. When the material is examined macroscopically, the presence of all dielectric dipoles will contribute to the overall net polarization *P* in a material.

$$P_{\text{net}} = P_{\text{electronic}} + P_{\text{ionic}} + P_{\text{molecular}} + P_{\text{interfacial}} \quad (4)$$

The individual dielectric dipoles can be characterized according to their length and time scale as electronic, ionic, molecular (dipole), and interfacial (space-charge) polarization as given in Eq. (4). All these mechanisms contribute to the overall permittivity 'ε' (also known as short range conductivity) to account for the presence of polarization *P* in the material.

Most materials show frequency dependent dielectric properties, because slower mechanisms present in the material fail to respond and contribute to the dielectric storage ($\varepsilon^{'}$) when the frequency becomes large. The dielectric properties can also show a dependence of temperature, applied field, crystal structure, impurities and defects present in the material [51] [52]. The frequency and temperature dependent dielectric measurements can give insight into the molecular structure of the polymer composite including the effects of added ceramic filler and their grain boundaries [53]. The contribution of polymer/ceramic interfaces, electrode effects and dynamics of charge carriers in the material can by analyzed using complex impedance analysis. The complex electric modulus analysis can be employed to explore the carrier hopping rate, relaxation phenomena in the polymer composite system.

It is to be noted that the relaxation process in heterogeneous polymer–ceramic system involves the oscillation of segmented polymer chains and dipoles (ionic polarization) present in the ceramic system. In addition to these two, the electrode effects (if present), interfacial charge transfer and polaron hopping (space-charge polarization) also contribute to the relaxation processes.

3.4 Frequency-dependent dielectric permittivity

The frequency-dependent dielectric properties of PVDF nanofibers and PVDF–$BaTiO_3$ nanofibrous composites were compared between the temperature range of 100–180 °C. The frequency dependence of real ($\varepsilon^{'}$) and imaginary part (ε'') of the complex dielectric permittivity between the temperature range of (100–180 °C) are presented in Figs. 4 and 5, respectively. The frequency-dependent real part ($\varepsilon^{'}$) of the complex permittivity values are higher for PVDF–$BaTiO_3$ nanofibrous composite compared to the neat PVDF as in Fig. 4a. The observed increase in value is due to the contribution from increased interfacial polarization at the PVDF–$BaTiO_3$ interface.

For the PVDF–$BaTiO_3$ nanofibrous composite in Fig. 4b, there is also an increase in dielectric permittivity at the frequency range of 20–10^3 Hz after 150 °C. This increase in $\varepsilon^{'}$ values after 150 °C is due to the presence of $BaTiO_3$ particles. Further, in Fig. 5a we can see a considerable increase in the loss factor (ε'') for PVDF nanofibers after 130 °C in the frequency range from 10^4 to 10^6 Hz. Since, the melting temperature of PVDF is around 170–180 °C and after 130 °C, the PVDF molecules tend to rotate and vibrate due to the increase in thermal energy, causing the ε'' to increase, whereas in case of PVDF–$BaTiO_3$ system in Fig. 5b, the loss factor (ε'') found to decrease with respect to frequency. Although the loss factor (ε'') value increases with temperature, the decrease in loss factor with frequency response can be attributed to the particle-induced crystallization, which causes the polymer to crystallize around $BaTiO_3$ particles leading to restricted motion. The particle-induced crystallization is due to heterogeneous nucleation and crystallization [54, 55]. However, in this case, since, the electrospinning offers local poling, a combination of homogeneous nucleation (electric field induced crystallization) and heterogeneous crystallization occurs in the PVDF–$BaTiO_3$ system.

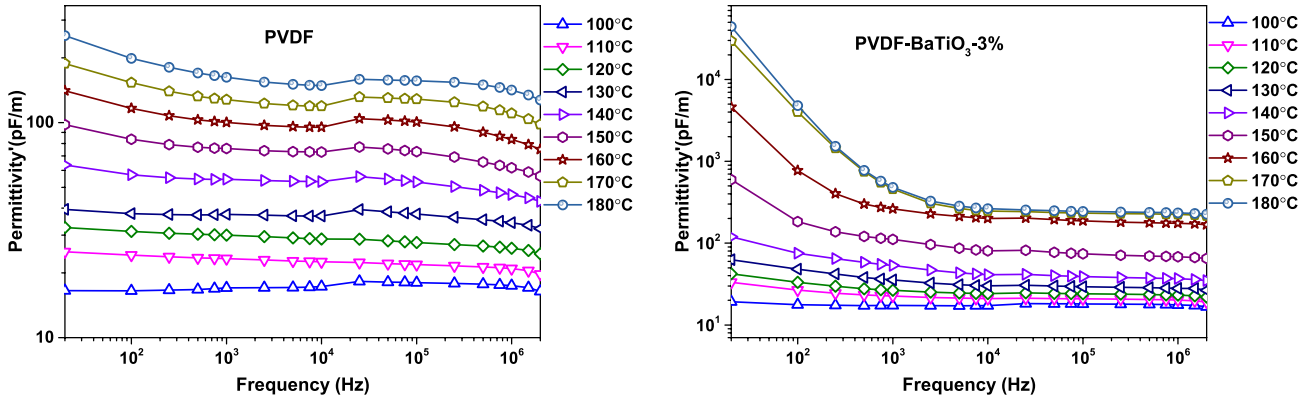

(a) PVDF nanofonibers **(b)** PVDF-$BaTiO_3$-3% nanofibrous composite

Fig. 4 Iso-thermal frequency variation of real part of the permittivity (ε') at different temperatures

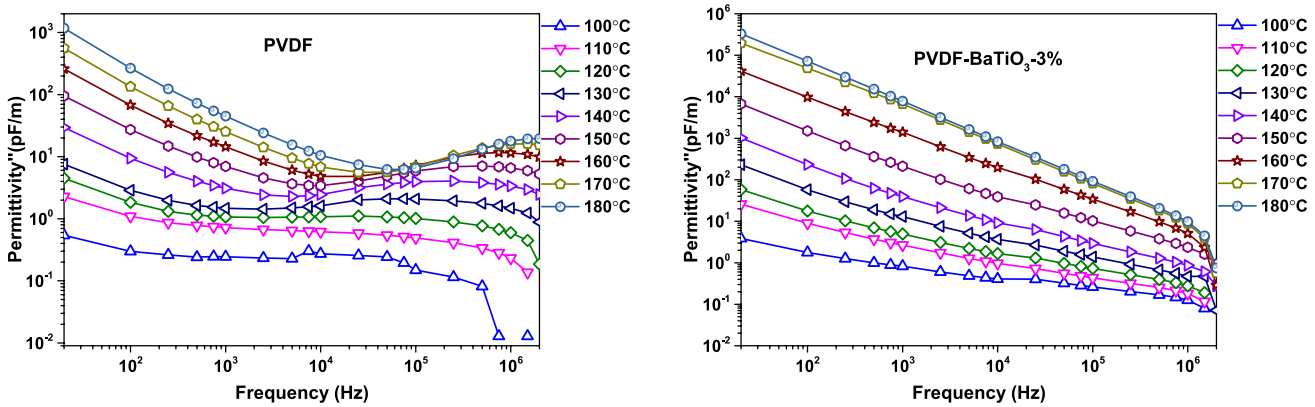

(a) PVDF nanofibers **(b)** PVDF-$BaTiO_3$-3% nanofibrous composite

Fig. 5 Iso-thermal frequency variation of imaginary part of the permittivity (ε'') at different temperatures

3.5 Impedance behavior

The impedance (Z^*) of a material can be explained using complex numbers [7] having both magnitude $|Z|$ and phase angle ϕ as follows

$$Z^*(\omega) = |Z|\ \cos\phi - j\ |Z|\ \sin\phi \tag{5}$$

The complex impedance (Z^*) consisting of real and imaginary parts of the complex number and can be used to explain the resistive behavior of the material in response to applied frequency. The impedance data in the complex plane can be represented using the following formalisms which are related to each other as follows

$$Z^* = Z' - Z'' = \frac{1}{j\ \omega\ C_0\ \varepsilon^*} \tag{6}$$

$$M^* = M' - j\ M'' = \frac{1}{\varepsilon^*} = j\ \omega\ C_0\ Z^* \tag{7}$$

$$Y^* = Y' - j\ Y'' = \frac{1}{Z^*} = j\ \omega\ C_0\ \varepsilon^* \tag{8}$$

$$\varepsilon^* = \varepsilon' + j\ \varepsilon'' = \frac{1}{j\ \omega\ C_0\ Z^*} \tag{9}$$

where $Z^*M^*Y^*\varepsilon^*$ are complex quantity having real and imaginary parts of impedance, electric modulus, admittance and dielectric permittivity, respectively. The j is imaginary factor, C_0 is capacitance of vacuum [56] and ω is angular frequency ($2\pi f$).

The real (Z') and imaginary (Z'') parts of the impedance are associated with the existence of resistor (in phase) and capacitor (out of phase) with the applied AC signal. The resistive (Z') and reactive part (Z'') of

impedance can be expressed in terms of dielectric permittivity as follows.

$$Z' = \frac{1}{2\,\pi\, f\, C_0}\,\frac{\varepsilon''}{\varepsilon'^2 + \varepsilon''^2} = R \tag{10}$$

$$Z'' = \frac{1}{2\,\pi\, f\, C_0}\,\frac{\varepsilon'}{\varepsilon'^2 + \varepsilon''^2} = \frac{-j}{\omega C} \tag{11}$$

where R and C are associated with resistor and capacitor, respectively. The frequency dependence of impedance resistive part (Z') and reactive part (Z'') of PVDF nanofibers and PVDF–$BaTiO_3$ nanofibrous composites are given from the temperature range of 100–180 °C in supplemental Fig. S3 and supplemental Fig. S4.

The decrease in Z' (resistive part) value with increase in frequency in supplemental Fig. S3(a) can be attributed to the PVDF segmental molecules which are in resonance with applied frequency. For PVDF–$BaTiO_3$ nanofibrous composite, in supplemental Fig. S3(b), it is seen that at the temperature range from 100 to 120 °C, there is a monotonous decrease of Z' value with increase in frequency. From 130 °C, the Z' value is independent of frequency for up to 10^4 Hz. This is due to the contribution of resistance from $BaTiO_3$ grain boundaries. After 10^4 Hz, the Z' becomes dependent of frequency. As the temperature increases, the Z' value decreases. For the composite in supplemental Fig. S3(b), the higher value of Z' at lower frequencies denote larger polarization contribution from $BaTiO_3$.

The frequency dependent Z'' plot of PVDF is given in supplemental Fig. S4(a) indicates a slight increase in Z'' value from 160 to 180 °C up to 100 Hz, after 100 Hz, the Z'' value shows a decreasing trend similar to the temperature range from 100 to 150 °C. This slight increase in Z'' value can be attributed to PVDF's melting temperature causing an increase in movement of segmental molecules from 160 to 180 °C. In case of PVDF–$BaTiO_3$ system in supplemental Fig. S4(b), there is a slight increase in Z'' value around 100 Hz, but start decreasing after 150 °C. The slight increase in Z'' value can be attributed to the temperature-dependent dipole oscillation in $BaTiO_3$. To get further insight into the dielectric relaxation behavior, Z' versus Z'' are plotted as a Nyquist plot and presented in the following section.

3.6 Complex impedance plots and equivalent circuits

The displacement of electric charge in a material can take place by two different charge transport mechanisms, (i) by polarization in which the charge motion is localized and confined and (ii) charge transport occurs by diffusion for longer length scales. The motion of electric charge in the PVDF–$BaTiO_3$ composite system can be studied by plotting the imaginary part versus the real part of the complex impedance as Nyquist plots (Fig. 6).

The complex impedance of a dielectric material sandwiched between the two parallel metallic plate configuration can be explained with parallel RC (Resistance-Capacitance) circuit.

The semicircular shape of the curve on the complex impedance plane, as shown in Fig. 6 can be understood with equivalent circuits [57]. At low frequencies, the impedance of the capacitor/dielectric material is large; therefore, the majority of the current is flowing through the resistor. As the temperature and frequency increases, efficient charge transfer takes place, leading to a decrease in impedance eventually reaching close to zero impedance. As the temperature gets close to the melting point of the PVDF, the diffusion of charge carriers takes place which is observed as a small tail denoted by a leaky circuit in Fig. 6d. The well-formed semicircular arc in the temperature range (130–150 °C) in Fig. 6c, indicates grain effect due to the presence of $BaTiO_3$.

From 160 to 180 °C in PVDF nanofibers in Fig. 6b, a single semicircle forms as temperature increases, which indicates that only one primary mechanism is responsible for the electrical conduction within the sample between the temperature range of 160–180 °C. In other words, the absence of other semicircles in the complex impedance plots suggests that the conduction is due to oscillation of the segmental molecules indicating the dominance of bulk contributions in PVDF nanofibrous membrane. It is also observed that Fig. 6b, as the temperature increases around 170 °C, the intercept points on the real axis shift towards the origin, indicating a decrease in the bulk resistance. This can be attributed to the melting temperature of PVDF, which causes the resistive part of impedance to decrease.

When PVDF–$BaTiO_3$ was examined in Fig. 6c, d, the intercept points on the real axis start shifting towards the origin from 140 °C onwards, indicating contribution of $BaTiO_3$ grains leading to decrease in the resistive property. In addition, the semicircle has the real-axis intercept at the end, denoting bulk electrolyte resistance. Here, the electrolyte being the nanofibrous composite sandwiched between the two parallel plate electrodes.

For PVDF–$BaTiO_3$ nanofibrous composite in Figs. 6c, d, the radii of the semicircles were decreasing with the increase in temperature, representing the distribution of relaxation times and decrease in the resistivity of the material with a deviation from the ideal Debye type relaxation. The deviation of ideal Debye type relaxation can be attributed to the $BaTiO_3$ grain boundary contribution. In other words, the addition of $BaTiO_3$ to PVDF causes the trapping of charges at the interface that diffuse after the PVDF melting temperature. This does not occur in the pure PVDF without $BaTiO_3$

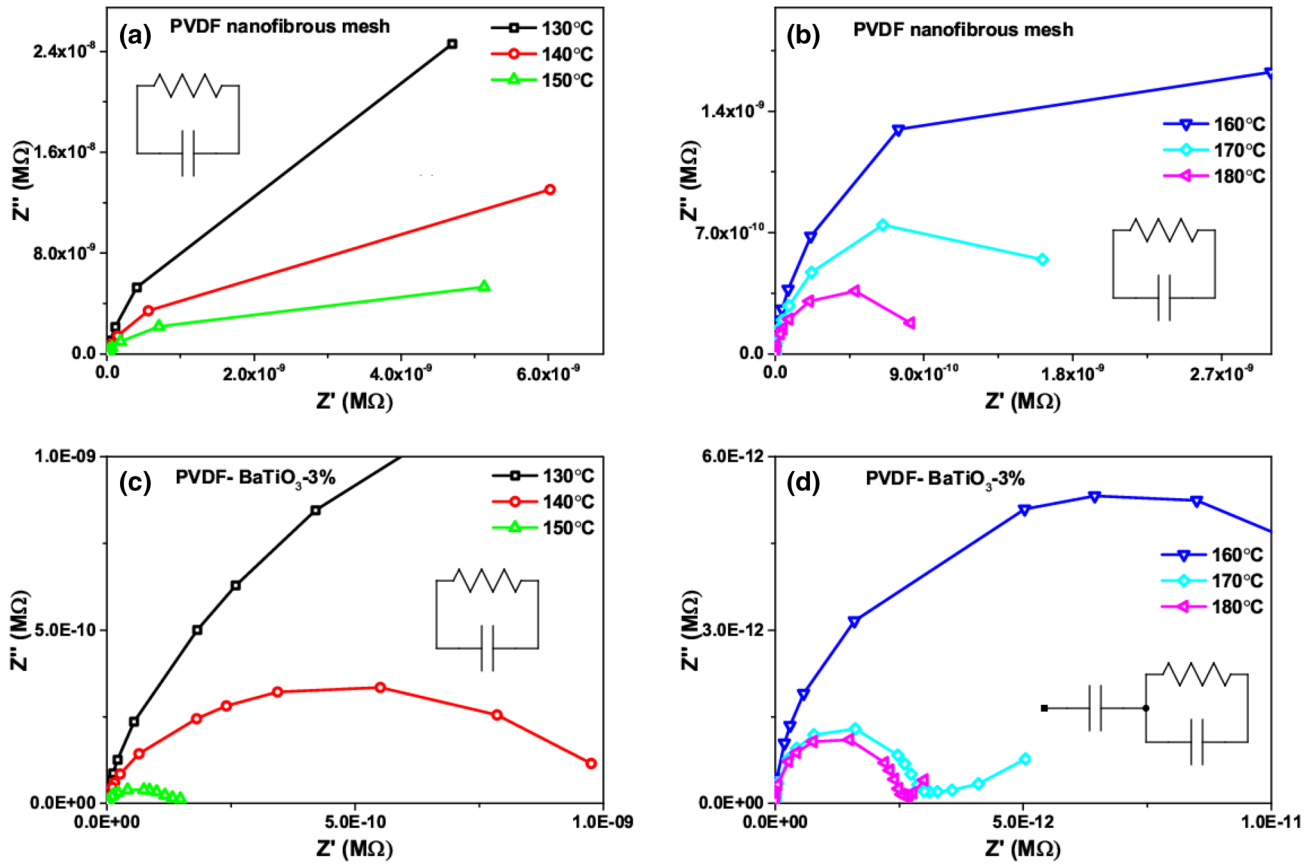

Fig. 6 Complex impedance plots for **a** Electrospun PVDF mesh (130–150 °C), **b** Electrospun PVDF mesh (160–180 °C), **c** PVDF–$BaTiO_3$-3% nanofibrous composite mesh (130–150 °C), **d** PVDF–$BaTiO_3$-3% nanofibrous composite mesh (160–180 °C)

providing a mechanistic contribution to polarization of $BaTiO_3$.

3.7 Electric modulus analysis

To probe the interfacial polarization and dielectric relaxation effects in composites, complex electric modulus formalism [58] was used. The complex electric modulus formalism can also be used to study the dielectric relaxation phenomena in many polymer systems [17, 59–61]. The complex electric modulus (M^*) can be defined in terms of reciprocal of complex dielectric permittivity (ε^*) as

$$M^* = \frac{1}{\varepsilon^*} \tag{12}$$

The complex electric modulus constitutes real (M') and imaginary part (M'').

$$M^* = M' + M'' = j\,\omega\,C_0\,Z^* \tag{13}$$

In the above equation, ω is angular frequency ($\omega = 2\pi f$), C_0 is capacitance of vacuum and Z^* is complex impedance.

The real part (M') and imaginary part (M') of electric modulus (M^*) can be expressed in terms of real (ε') and imaginary part (ε'') of dielectric permittivity as follows:

$$M' = \frac{\varepsilon'}{\varepsilon'^2 + \varepsilon''^2} \tag{14}$$

$$M'' = \frac{\varepsilon''}{\varepsilon'^2 + \varepsilon''^2} \tag{15}$$

The calculated M' and M'' from Eqs. (14) and (15) are plotted as a function of frequency at different temperatures in Figs. 7 and 8. For PVDF, the value of M' is very small in the low frequency region, but as frequency increases, the electric modulus (M') increases. As temperature increases from 120 to 180 °C in Fig. 7a, b, the electric modulus M' decreases for both PVDF nanofibers and PVDF–$BaTiO_3$ nanofibrous composite. In the electric loss modulus spectra M'' of PVDF nanofibers in Fig. 8a, a relaxation process can be identified by the peak in the M'' curves at 160–180 °C. The M'' peaks for the relaxation

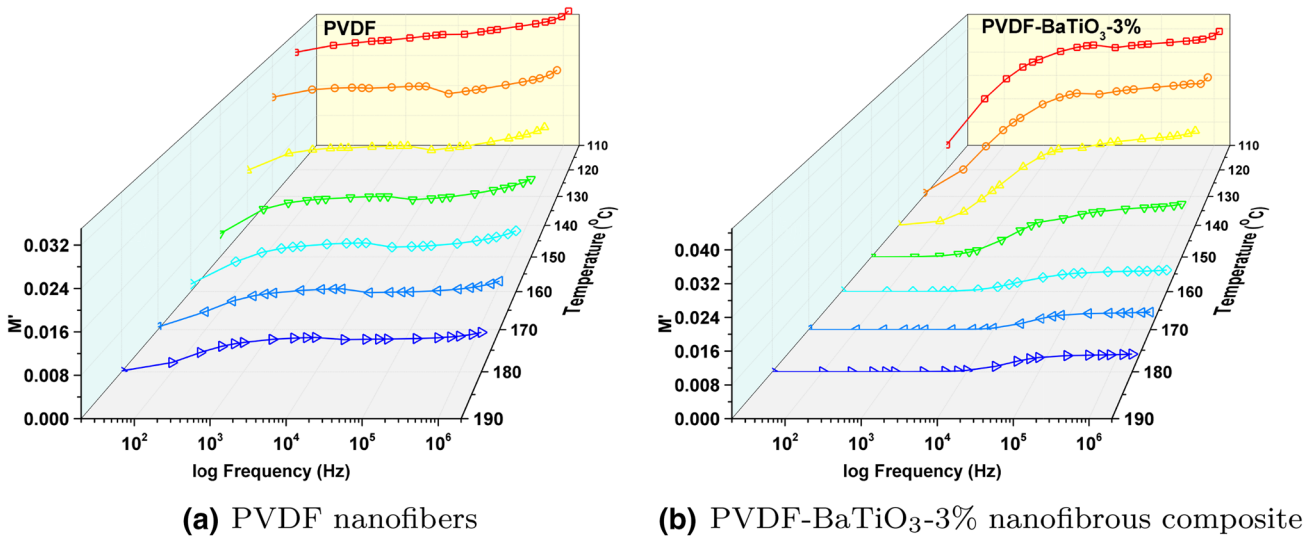

Fig. 7 The variation of real part of the complex electric modulus, $M'(\omega)$, as a function of frequency and temperature

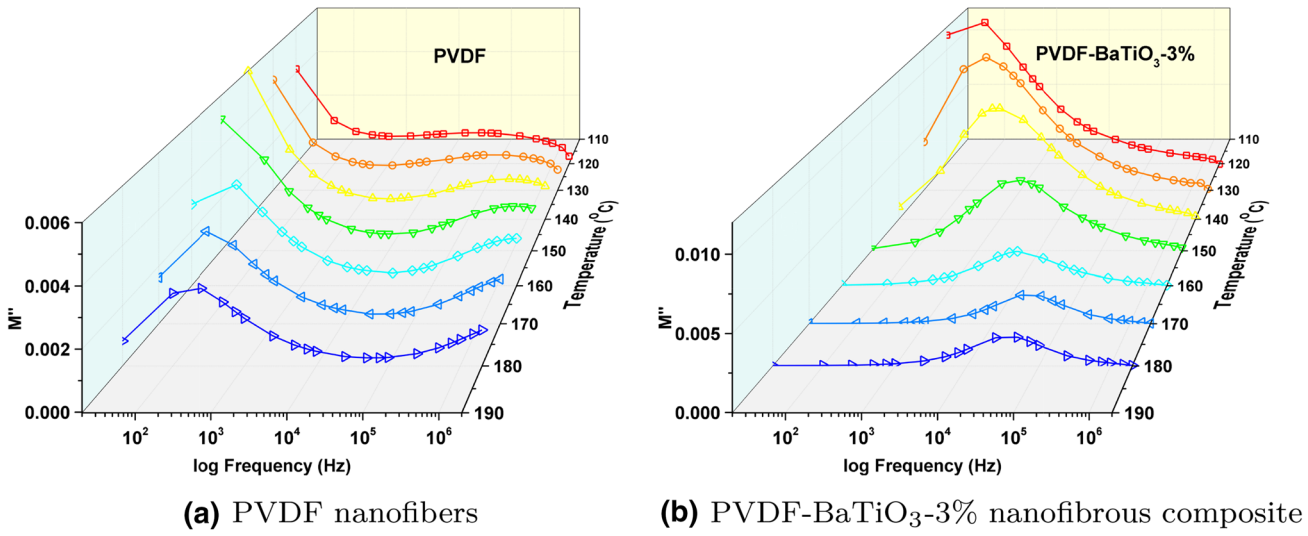

Fig. 8 The variation of imaginary part of the complex electric modulus, $M''(\omega)$, as a function of frequency and temperature

process for PVDF and PVDF–$BaTiO_3$ in Fig. 8, shifts to higher frequency with the rise in temperature.

For PVDF–$BaTiO_3$ nanofibrous composite in Fig. 8b, the relaxation peaks can be observed from temperature 120 to 180 °C. The additional relaxation peaks in the M'' spectra can be attributed to Maxwell–Wagner–Sillars (MWS) polarization which occurs in the interface between non-homogenous/heterogeneous materials where the materials have different dielectric permittivity [62]. MWS model [63, 64] can also be used for explaining the polarization in semicrystalline polymers like PVDF, where the permittivity of crystalline and amorphous phase differs [65].

3.8 Holstein polarons with Arrhenius plots

The scaling behavior of the samples was studied by plotting M''/M''_{max} versus $log_{10}f/f_{max}$ at different temperatures. All these curves overlap in one master modulus curve which gives insight into the dielectric response of the material. The normalized master curves are shown in Fig. 9a (PVDF mesh) and Fig. 9b (PVDF–$BaTiO_3$ nanofibrous composite mesh). In Fig. 9b, there is a slight shift in the peak pattern at higher frequency region, showing asymmetric behavior at right side of the peak where it becomes slightly temperature dependent. Therefore, except at high frequencies, a single type relaxation is observed in

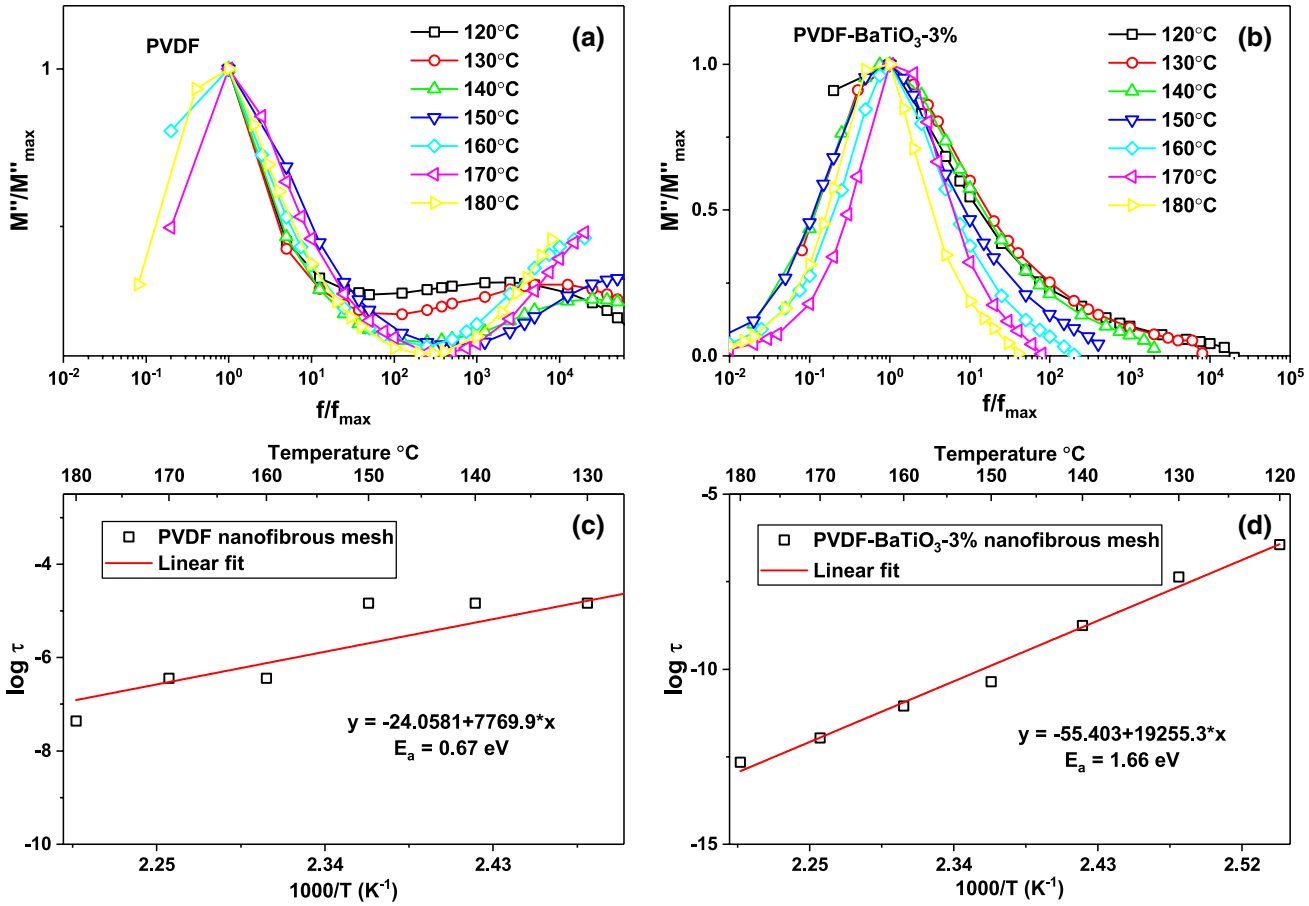

Fig. 9 Normalized master curves of **a** Electrospun PVDF mesh **b** PVDF–$BaTiO_3$-3% nanofibrous composite mesh and Arrhenius plots of **c** Electrospun PVDF mesh **d** PVDF–$BaTiO_3$-3% nanofibrous composite mesh

the PVDF–$BaTiO_3$ system. This kind of asymmetric behavior is mostly governed by disorder/inhomogeneities in the materials [56] resulting in non-Debye type relaxation behavior.

Unlike metals, the PVDF polymer and $BaTiO_3$ have narrow band structures due to the confinement of electrons. Due to the narrow band structure, there is a considerable decrease in mobility of charge carriers. So, the confined electron will distort or polarizes the crystal lattice [66]. This creates a binding force between electron and distorted lattice leading to the formation of quasiparticle called polaron [67].

Typically, the polarons are classified as large and small polarons, according to the binding forces and the environment in which the charge carrier resides. The strong polarons are characteristics of ionic compounds in which a strong binding force exists between charge carrier and the lattice leading to polaron having large effective mass [68]. Usually, the spatial extent of these large polarons exceeds the lattice constant and are called Fröhlich polarons [69]. The small polarons are called Holstein polarons [70, 71] where the spatial extent of polarization is about the size of the lattice constant and typically found in organic materials in which only a small amount of energy is required to make a distortion in the structure. The hopping behavior of large polarons is quite similar to that of electrons or the holes, while small polarons follow a thermally activated Arrhenius-like hopping process whose exponent depends of the binding energy and the temperature [72]. The small polarons can also conduct through tunneling process, which depends on the crystal structure and composition of the material.

The M'' versus f curves which shifts towards higher frequency with increase in temperature. The maximum angular frequency $\omega_{max}(2\pi f_{max})$ corresponds to M''_{max} (maximum value of M''), is the reciprocal of the relaxation time, τ_M:

$$\omega_{max} = \frac{1}{\tau_M} \tag{16}$$

where τ_M is the relaxation time calculated from electric modulus. At different temperatures, this relaxation

frequency ω_{max} is different and increases with increase in temperature. This kind of temperature dependence follows Arrhenius-type behavior and can be expressed as follows:

$$\tau = \tau_0 \exp\left(\frac{E_a}{K_B T}\right) \quad (17)$$

where τ_0 is the pre-exponential factor, K_B is the Boltzmann's constant ($\sim 8.617 \times 10^{-5} eV$), T is temperature in Kelvin and E_a is the activation energy. The pre-exponential factor τ_0 and activation energy E_a were calculated by solving the above equation. Taking ln on both sides of Eq. (17) we get,

$$\ln \tau = \ln \tau_0 + \ln exp\left(\frac{E_a}{K_B T}\right) \quad (18)$$

$$\ln \tau = \ln \tau_0 - \left(\frac{E_a}{K_B T}\right) \quad (19)$$

Rearranging Eq. (19),

$$\ln \tau = \left(\frac{-E_a}{K_B}\right)\frac{1}{T} + \ln \tau_0 \quad (20)$$

Equation (20) fits the linear regression equation $y = mx + c$, from which, the pre-exponential factor τ_0 and activation energy E_a were calculated.

The observed fitting parameters τ_0 and E_a for PVDF nanofibers and PVDF–$BaTiO_3$ nanofibrous composite are listed in Table 1. The calculated activation energy corresponds to thermally activated small polaron (Holstein polaron) hopping. The observed increase in value of the activation energy of PVDF–$BaTiO_3$ nanofibrous composite is due to the increase in binding energy of charge carrier with the ionic $BaTiO_3$ compound. The decrease in relaxation time (τ_M) with increase in temperature can be attributed to the enhancement of mobility of charge carriers occurring at higher temperatures. The polaron hopping effect can be attributed to the temperature-dependent relaxation behavior at the high frequency region.

Table 1 Relaxation time and activation energy for PVDF nanofibers and PVDF–$BaTiO_3$ nanofibrous composite

Sample	Relaxation at infinite time (τ_0)	Activation energy (E_a) (eV)
PVDF mesh	3.56E−11	0.67
PVDF–$BaTiO_3$-3%	3.10E−21	1.66

3.9 Thermodynamic properties

The particle-induced crystallization was studied using DSC analysis. Figure 10 shows the second heating and second cooling curves for PVDF and PVDF–$BaTiO_3$ nanofibrous composite. DSC results of the pure PVDF nanofibers and PVDF–$BaTiO_3$ nanofibrous composite are summarized in Table 2. Melting temperature (T_m), melting enthalpy (ΔH_m), melt crystallization temperature (T_{mc}), and melt crystallization enthalpy (ΔH_{mc}) were obtained from the second-heating and second-cooling thermograms.

PVDF nano-fibrous mesh has the melting temperature 159.72 °C and melting enthalpy of 0.5546 J/g. The 3%

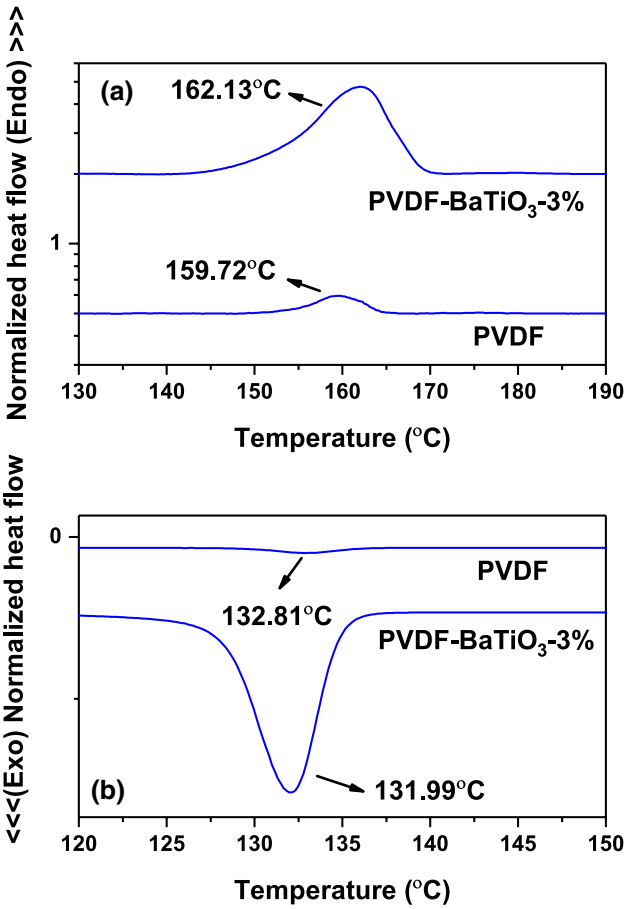

Fig. 10 Differential scanning calorimetry. **a** Second heating curves and **b** second cooling curves

Table 2 Differential scanning calorimetry results from second-heating and second-cooling thermograms

Sample	T_m(°C)	ΔH_m (J/g)	T_{mc}(°C)	ΔH_{mc} (J/g)	X_c (%)
PVDF mesh	159.72	0.5546	132.81	− 1.0624	0.53
PVDF–$BaTiO_3$-3%	162.13	38.8208	131.99	− 50.8864	36.97

addition of $BaTiO_3$ causes an increase in melting temperature of 162.13 °C and corresponding melting enthalpy (ΔH_m) increased significantly to 38.8208 J/g. PVDF nanofibrous mesh has the crystallization temperature (T_{mc}) of 132.88 °C. The corresponding degree of crystallinity (X_c) of the samples were determined by

$$X_c = \left(\frac{\Delta H_m}{\Delta H_0}\right) \times 100\% \quad (21)$$

where ΔH_0 is the enthalpy of crystalline PVDF (105 J/g) [73]. The degree of crystallinity was found to be 0.53 and 36.97 for PVDF and PVDF–$BaTiO_3$-3%, respectively. The increase in crystallinity compliments the heating scan results where increase in enthalpy values was observed by the addition of 3 % $BaTiO_3$. In addition to electrospinning, the 3% addition of $BaTiO_3$ particles act as a nucleating agent for the crystallization of PVDF in the composite.

The increased crystalline nature of the PVDF can also be viewed from materials processing aspect. By applying electric field in excess of 1 MV/cm, there is a residual polarization in crystal phase of PVDF [74]. The particle-induced polarization is also enhanced by applying electric field (20 kV during electrospinning process), which causes the local poling, leading the polymers to align themselves in an isotactic configuration leading to increased rotational polarization in polymer composite. This combination of field-induced and dielectric filler-induced polarization justifies the increased crystallization behavior of PVDF–$BaTiO_3$ composite, observed from thermodynamic studies.

3.10 Impact sensing

The impact sensing results are shown as Force versus charge generated plot in supplemental Fig. S6. The results in Table 3 indicated that the higher voltage generated in the composite structure is due to the combination of increase in particle-induced crystallization and increased interfacial polarization due to the presence of $BaTiO_3$ particles in the system. The nanofibrous structure offers increased interfacial adhesion between the piezoelectric material and electrodes which facilitates the efficient charge generation and transportation.

Table 3 Impact force and Voltage generated for PVDF nanofibers and PVDF–$BaTiO_3$ nanofibrous composite

Sample	Impact force (N)	Voltage generated (mV)
PVDF mesh	37.3333	250
PVDF mesh	55.1111	340
PVDF mesh	85.3333	410
PVDF–$BaTiO_3$-3%	24.0000	420
PVDF–$BaTiO_3$-3%	33.7778	640
PVDF–$BaTiO_3$-3%	88.8889	1700

The constitutive relationship for direct piezoelectric effect can be written as

$$D = d\sigma + \mu^{\sigma} E \quad (22)$$

where D is electric displacement/flux density (C/m^2), d is piezoelectric constant/electromechanical coupling constant (C/N or m/V), σ is stress (N/m^2), μ is permittivity (F/m), E is electric field intensity (V/m or N/C) and μ^{σ} denotes permittivity at constant stress.

The overall electric displacement (D) (charge generated in the material) of the piezoelectric materials constitutes applied stress, permittivity and electric field intensity. The observed increase in the piezoelectricity of the prepared PVDF–$BaTiO_3$ electrospun composite system can be attributed to the following key factors 1. Increase in interfacial polarization between PVDF and $BaTiO_3$ which in turn increases the permittivity and 2. Efficient charge transport due to small polaron hopping effect.

4 Conclusion

The major outcomes of this work are summarized below which will provide a framework to study the charge transport properties in the nanocomposite/hybrid system:

1. The PVDF–$BaTiO_3$ interface was studied for the first time, to explore the interfacial nature of the compound. The experimental findings are well supported by the DFT and Bader charge analysis.
2. The DFT calculations and Bader charge analyses showed that the interfacial charge transfer occurs between PVDF and PVDF–$BaTiO_3$, leading to the increased polarization of the nanocomposite.
3. The frequency and temperature dependent dielectric characterization agrees with the DFT results showing an increase in dielectric permittivity with PVDF–$BaTiO_3$ nanocomposite. Complex impedance analysis of the composite revealed the decrease in bulk resistance with increase in temperature.
4. Electric modulus analysis of the PVDF–$BaTiO_3$ system showed a temperature-dependent Arrhenius-type behavior. Further, the interfacial polarization is confirmed with the increased activation energy for the PVDF–$BaTiO_3$ system. The $BaTiO_3$ also contributes to the small polaron hopping effect which enhances the charge carrier dynamics and thereby piezoelectric property as evidenced in impact sensing analysis.

5. The observed scaling of electric modulus master curves at different temperatures indicates that the transport dynamics of charge carriers in PVDF–$BaTiO_3$ -3% is almost temperature independent across the relaxation regime and temperature dependent only at higher frequencies where the mobility of charge carriers increases. The relaxation regime was supported by DSC analysis and crystallization behavior.
6. The proposed mechanistic consequences of $BaTiO_3$ in increasing interfacial polarization and increasing mobility of charges at higher frequencies (short times) is confirmed through the impact measurements which show a significant increase in charge generation per increment in force. This indicates that the prepared electrospun nanofibrous piezoelectric composite can find application as embedded flexible impact sensing material for use in head wear for athletes and army personnel and in biomechanical energy harvesting applications.

Acknowledgements The author would like to acknowledge Mechanical and energy engineering department and Materials research facility at University of North Texas for fabrication and characterization of materials.

Compliance with ethical standards

Conflict of interest The authors declare that there is no conflict of interest regarding the publication of this paper.

References

1. Fiorillo AS, Pullano SA, Bianco MG, Critello CD (2019) Bioinspired US sensor for broadband applications. Sens Actuat A Phys 294:148–153
2. Mo X, Zhou H, Li W, Xu Z, Duan J, Huang L, Hu B, Zhou J (2019) Piezoelectrets for wearable energy harvesters and sensors. Nano Energy 65:104033
3. Stadlober B, Zirkl M, Irimia-Vladu M (2019) Route towards sustainable smart sensors: ferroelectric polyvinylidene fluoride-based materials and their integration in flexible electronics. Chem Soc Rev 48(6):1787–1825
4. Dagdeviren C, Joe P, Tuzman OL, Park KI, Lee KJ, Shi Y, Huang Y, Rogers JA (2016) Recent progress in flexible and stretchable piezoelectric devices for mechanical energy harvesting, sensing and actuation. Extreme Mech Lett 9:269–281
5. Chinnam KC, Fabriani F, Giovanna I, Lanzara G (2018) Electrospun PVDF miniaturized muscles for bio inspired morphing materials. In: ASME 2018 conference on smart materials, adaptive structures and intelligent systems, San Antonio
6. Guo W, Tan C, Shi K, Li J, Wang XX, Sun B, Huang X, Long YZ, Jiang P (2018) Wireless piezoelectric devices based on electrospun PVDF/$BaTiO_3$ NW nanocomposite fibers for human motion monitoring. Nanoscale 10(37):17751–17760
7. Barsoukov E, Macdonald JR (2005) Impedance spectroscopy: theory, experiment, and applications. Wiley, New York
8. Chen X, Han X, Shen QD (2017) PVDF-based ferroelectric polymers in modern flexible electronics. Adv Electron Mater 3(5):1600460
9. Yan J, Liu M, Jeong YG, Kang W, Li L, Zhao Y, Deng N, Cheng B, Yang G (2019) Performance enhancements in poly(vinylidene fluoride)-based piezoelectric nanogenerators for efficient energy harvesting. Nano Energy 56:662–692
10. Wei H, Wang H, Xia Y, Cui D, Shi Y, Dong M, Liu C, Ding T, Zhang J, Ma Y, Wang N, Wang Z, Sun Y, Wei R, Guo Z (2018) An overview of lead-free piezoelectric materials and devices. J Mater Chem C 6(46):12446–12467
11. Arbatti M, Shan X, Cheng ZY (2004) New high-dielectric-constant polymer-ceramic composites. MRS Proc 847:13–58
12. Corral-Flores V, Bueno-Baques D (2011) Flexible ferroelectric $BaTiO_3$-PVDF nanocomposites. InTech
13. Eliseev EA, Morozovska AN (2009) General approach for the description of size effects in ferroelectric nanosystems. J Mater Sci 44(19):5149–5160
14. Ramrus A, White W, Brown E, Haskell K (1982) Use of PVDF film in high energy density capacitors. In: Conference on electrical insulation and dielectric phenomena. Annual report. IEEE, pp 549–556
15. Fan FR, Tang W, Wang ZL (2016) Flexible nanogenerators for energy harvesting and self-powered electronics. Adv Mater 28(22):4283–4305
16. Surmenev RA, Orlova T, Chernozem RV, Ivanova AA, Bartasyte A, Mathur S, Surmeneva MA (2019) Hybrid lead-free polymer-based nanocomposites with improved piezoelectric response for biomedical energy-harvesting applications: a review. Nano Energy 62:475–506
17. Chanmal CV, Jog JP (2008) Dielectric relaxations in PVDF/$BaTiO_3$ nanocomposites. Express Polym Lett 2(4):294–301
18. Sharma M, Quamara JK, Gaur A (2018) Behaviour of multiphase PVDF in (1–x)PVDF/(x)$BaTiO_3$ nanocomposite films: structural, optical, dielectric and ferroelectric properties. J Mater Sci Mater Electron 29(13):10875–10884
19. Yu K, Wang H, Zhou Y, Bai Y, Niu Y (2013) Enhanced dielectric properties of $BaTiO_3$/poly(vinylidene fluoride) nanocomposites for energy storage applications. J Appl Phys 113(3):34105
20. Fu J, Hou Y, Zheng M, Wei Q, Zhu M, Yan H (2015) Improving dielectric properties of PVDF composites by employing surface modified strong polarized $BaTiO_3$ particles derived by molten salt method. ACS Appl Mater Interfaces 7(44):24480–24491
21. Olmos D, Gonzalez-Gaitano G, Vela R, Cordoba L, Gonzalez-Benito J, Kholkin AL (2012) Flexible PVDF-$BaTiO_3$ nanocomposites for pressure sensors. In: Proceedings of ISAF-ECAPD-PFM 2012. IEEE, Aveiro, pp 1–3
22. Hao YN, Wang XH, O'Brien S, Lombardi J, Li LT (2015) Flexible $BaTiO_3$/PVDF gradated multilayer nanocomposite film with enhanced dielectric strength and high energy density. J Mater Chem C 3(37):9740–9747
23. Bouharras FE, Raihane M, Silly G, Totee C, Ameduri B (2019) Core-shell structured poly(vinylidene fluoride)-grafted-$BaTiO_3$ nanocomposites prepared via reversible addition-fragmentation chain transfer (RAFT) polymerization of VDF for high energy storage capacitors. Polym Chem 10(7):891–904
24. Bodkhe S, Turcot G, Gosselin FP, Therriault D (2017) One-step solvent evaporation-assisted 3D printing of piezoelectric PVDF nanocomposite structures. ACS Appl Mater Interfaces 9(24):20833–20842
25. Phatharapeetranun N, Ksapabutr B, Marani D, Bowen JR, Esposito V (2017) 3D-printed barium titanate/poly-(vinylidene fluoride) nano-hybrids with anisotropic dielectric properties. J Mater Chem C 5(47):12430–12440

26. Gerhard-Multhaupt R (2002) Less can be more holes in polymers lead to a new paradigm of piezoelectric materials for electret transducers. IEEE Trans Dielectrics Electric Insul 9(5):850–859
27. Zhang Y (2006) In situ fatigue crack detection using piezoelectric paint sensor. J Intell Mater Syst Struct 17(10):843–852
28. Laflamme S, Kollosche M, Connor JJ, Kofod G (2013) Robust flexible capacitive surface sensor for structural health monitoring applications. J Eng Mech 139(7):879–885
29. Ramesh D, D'Souza NA (2018) One-step fabrication of biomimetic PVDF-$BaTiO_3$ nanofibrous composite using DoE. Mater Res Express 5(8):085308
30. Lang C, Fang J, Shao H, Ding X, Lin T (2016) High-sensitivity acoustic sensors from nanofibre webs. Nat Commun 7:11108
31. Aliheidari N, Aliahmad N, Agarwal M, Dalir H (2019) Electrospun nanofibers for label-free sensor applications. Sensors 19(16):3587
32. Han W, Wang Y, Su J, Xin X, Guo Y, Long YZ, Ramakrishna S (2019) Fabrication of nanofibrous sensors by electrospinning. Sci China Technol Sci 62(6):886–894
33. Yang E, Xu Z, Chur LK, Behroozfar A, Baniasadi M, Moreno S, Huang J, Gilligan J, Minary-Jolandan M (2017) Nanofibrous smart fabrics from twisted yarns of electrospun piezopolymer. ACS Appl Mater Interfaces 9(28):24220–24229
34. Ponnamma D, Al Ali Al-Maadeed M (2019) Influence of $BaTiO_3$ /white graphene filler synergy on the energy harvesting performance of a piezoelectric polymer nanocomposite. Sustain Energy Fuels 3(3):774–785
35. Itoh A, Takahashi Y, Furukawa T, Yajima H (2014) Solid-state calculations of poly(vinylidene fluoride) using the hybrid DFT method: spontaneous polarization of polymorphs. Polym J 46:207
36. Stradi D, Jelver L, Smidstrup S, Stokbro K (2017) Method for determining optimal supercell representation of interfaces. J Phys Condens Matter 29(18):185901
37. Blöchl PE (1994) Projector augmented-wave method. Phys Rev B 50(24):17953–17979
38. Kresse G, Joubert D (1999) From ultrasoft pseudopotentials to the projector augmented-wave method. Phys Rev B 59(3):1758–1775
39. Mortensen JJ, Hansen LB, Jacobsen KW (2005) Real-space grid implementation of the projector augmented wave method. Phys Rev B 71(3):35109
40. Enkovaara J, Rostgaard C, Mortensen JJ, Chen J, Dułak M, Ferrighi L, Gavnholt J, Glinsvad C, Haikola V, Hansen HA, Kristoffersen HH, Kuisma M, Larsen AH, Lehtovaara L, Ljungberg M, Lopez-Acevedo O, Moses PG, Ojanen J, Olsen T, Petzold V, Romero NA, Stausholm-Møller J, Strange M, Tritsaris GA, Vanin M, Walter M, Hammer B, Häkkinen H, Madsen GKH, Nieminen RM, Nørskov JK, Puska M, Rantala TT, Schiøtz J, Thygesen KS, Jacobsen KW (2010) Electronic structure calculations with GPAW: a real-space implementation of the projector augmented-wave method. J Phys Condens Matter 22(25):253202
41. Monkhorst HJ, Pack JD (1976) Special points for Brillouin-zone integrations. Phys Rev B 13(12):5188–5192
42. Perdew JP, Burke K, Ernzerhof M (1996) Generalized gradient approximation made simple. Phys Rev Lett 77(18):3865–3868
43. Henkelman G, Arnaldsson A, Jónsson H (2006) A fast and robust algorithm for Bader decomposition of charge density. Comput Mater Sci 36(3):354–360
44. Tang W, Sanville E, Henkelman G (2009) A grid-based Bader analysis algorithm without lattice bias. J Phys Condens Matter 21(8):84204
45. Bader RFW (1994) Atoms in molecules: a quantum theory. Oxford University Press, Oxford
46. Sigmund P (1969) Theory of sputtering. I. Sputtering yield of amorphous and polycrystalline targets. Phys Rev 184(2):383–416
47. Shi N, Ramprasad R (2006) Atomic-scale dielectric permittivity profiles in slabs and multilayers. Phys Rev B 74(4):045318
48. Yu L, Ranjan V, Nardelli MB, Bernholc J (2009) First-principles investigations of the dielectric properties of polypropylene/metal-oxide interfaces. Phys Rev B 80(16):165432
49. Ruibal R, Ernst V (1965) The structure of the digital setae of lizards. J Morphol 117(3):271–293
50. Schneider CA, Rasband WS, Eliceiri KW (2012) NIH Image to ImageJ: 25 years of image analysis. Nat Methods 9(7):671–675
51. Ulrich RK (2003) Dielectric materials for integrated capacitors. In: Ulrich RK, Schaper LW (eds) Integrated passive component technology. IEEE Press, Wiley, Hoboken, NJ, pp 75–97
52. Blythe A (1979) Electrical properties of polymers, vol 1. Cambridge University Press, Cambridge
53. Gerhardt RR (1994) Impedance and dielectric spectroscopy revisited: distinguishing localized relaxation from long-range conductivity. J Phys Chem Solids 55(12):1491–1506
54. Li H, Yan S (2011) Surface-induced polymer crystallization and the resultant structures and morphologies. Macromolecules 44(3):417–428
55. Ning N, Fu S, Zhang W, Chen F, Wang K, Deng H, Zhang Q, Fu Q (2012) Realizing the enhancement of interfacial interaction in semicrystalline polymer/filler composites via interfacial crystallization. Prog Polym Sci 37(10):1425–1455
56. Jonscher AK (1977) The 'universal' dielectric response. Nature 267(5613):673–679
57. Aziz SB, Woo TJ, Kadir MFZ, Ahmed HM (2018) A conceptual review on polymer electrolytes and ion transport models. J Sci Adv Mater Dev 3(1):1–17
58. McCrum N (1967) Anelastic and dielectric effects in polymeric solids. Wiley, London
59. Hodge I, Eisenberg A (1978) Conductivity relaxation in an amorphous-iron-containing organic polymer. J Non-Cryst Solids 27(3):441–443
60. Starkweather HW, Avakian P (1992) Conductivity and the electric modulus in polymers. J Polym Sci Part B Polym Phys 30(6):637–641
61. Tsangaris GM, Psarras GC, Kouloumbi GM (1998) Electric modulus and interfacial polarization in composite polymeric systems. J Mater Sci 33(8):2027–2037
62. Mijović J, Lee H, Kenny J, Mays J (2006) Dynamics in polymer-silicate nanocomposites as studied by dielectric relaxation spectroscopy and dynamic mechanical spectroscopy. Macromolecules 39(6):2172–2182
63. Kremer F, Schönhals A (eds) (2003) Broadb and dielectric spectroscopy. Springer, Berlin
64. Sillars R (1937) The properties of a dielectric containing semiconducting particles of various shapes. J Inst Electric Eng 80(484):378–394
65. Arous M, Amor IB, Kallel A, Fakhfakh Z, Perrier G (2007) Crystallinity and dielectric relaxations in semi-crystalline poly(ether ether ketone). J Phys Chem Solids 68(7):1405–1414
66. Landau LD (1933) Electron motion in crystal lattices. Phys Z Sowjet 3:664
67. Pekar S (1946) Autolocalization of the electron in a dielectric inertially polarizing medium. Zhurnal Eksperimentalnoi i Teoreticheskoi Fiziki 16(4):335–340
68. Landau LD, Pekar SI (1948) Effective mass of a polaron. J Exp Theor Phys 18:419–423
69. Fröhlich H (1954) Electrons in lattice fields. Adv Phys 3(11):325–361
70. Holstein T (2000) Studies of polaron motion: part I. Mol Cryst Model Ann Phys 281(1):706–724
71. Holstein T (2000) Studies of polaron motion: part II. The "small" polaron. Ann Phys 281(1):725–773
72. Devreese JT (1996) Polarons. Wiley, New York

73. Nakagawa K, Ishida Y (1973) Annealing effects in poly(vinylidene fluoride) as revealed by specific volume measurements, differential scanning calorimetry, and electron microscopy. J Polym Sci Polym Phys 11(11):2153–2171
74. Davis GT, McKinney JE, Broadhurst MG, Roth SC (1978) Electric-field-induced phase changes in poly(vinylidene fluoride). J Appl Phys 49(10):4998–5002